Doppler-Free Absorption Spectroscopy and Implementation of a Λ-System for Electromagnetically Induced Transparency in Rubidium

Aleksandar Tuzlak
atuzlak@ethz.ch
ETH Zürich, D-PHYS
July 8, 2025

This experiment investigates light-matter interaction in rubidium atoms using Doppler-free absorption spectroscopy and electromagnetically induced transparency (EIT). By implementing a laser spectroscopy setup, the hyperfine structure of the D_1 line for ^{87}Rb and ^{85}Rb was resolved with sub-MHz precision. From the observed spectrum, transition frequencies, hyperfine splittings as well as doppler broadening and natural linewidth for the ^{87}Rb $5^2\mathrm{S}_{1/2} \to 5^2\mathrm{P}_{1/2}$ transition were extracted and compared to literature values and theoretical predictions. The compared values generally show strong agreement with the literature values and theory, with discrepancies being in the MHz range. Furthermore a Λ-system three-level system was realized to observe EIT. The EIT signal was found to shift under an applied magnetic field confirming the Zeeman effect and the corresponding Zeeman splitting. We conclude that the experiment was successful in demonstrating the principles of quantum optics, Doppler-free spectroscopy and EIT in rubidium atoms but extensive error analysis on the experiment setup to reduce systematic errors and more descriptive models for signal characterization will lead to more accurate results and aid in effectively quantifying the EIT phenomenon.

Quantum optics is the field of research that studies light-matter interaction at the quantum level. It is a fundamental aspect of modern physics with applications ranging from quantum computing to quantum communication. This allows us to perform atomic spectroscopy and then making use of it to manipulate an atomic ensamble in a coherent way in order to change the properties of atoms with laser light and magnetic fields.

This experiment focuses on probing and manipulating the internal state of rubidium (Rb) atoms with a relative natural abundance η of 27.83(2)% ^{87}Rb and 72.17(2)% ^{85}Rb. [1][2] Furthermore the full ground state electron configuration of Rb is $1s^2 2s^2 2p^6 3s^2 3p^6 3d^{10} 4s^2 4p^6 5s^1$ or, using the noble gas notation, $[\mathrm{Kr}]5s^1$ with a single $5s^1$ electron in the valence band resembling the energy-level structure of hydrogen. The internal energy states of ^{87}Rb are determined by the state of its valence electron completely described by its orbital angular momentum $\vec{L}$ and spin $\vec{S}$. Additionally, the spin-orbit coupling is given by

$$\mathcal{V}_{SO} = A_{fs}\vec{L}\vec{S} \tag{1}$$

where A_{fs} is the fine-structure coupling constant. This leads to the fine-structure splitting characterized by the total angular momentum $\vec{J} = \vec{L} + \vec{S}$. To specify the electronic states we use the Russel-Saunders notation. Hence for Rb one has a $5^2\mathrm{S}_{1/2}$ ground state and the two excited states $5^2\mathrm{P}_{1/2}$ and $5^2\mathrm{P}_{3/2}$. In this experiment we will investigate the optical transitions between the $5^2\mathrm{S}_{1/2}$ and the $5^2\mathrm{P}_{1/2}$ states, the so-called D_1 ($5^2\mathrm{S}_{1/2} \to 5^2\mathrm{P}_{1/2}$) line with an energy splitting of

$$\begin{aligned} &\Delta E = h \cdot \nu \\ &\rightsquigarrow \begin{cases} \Delta E_{D_1}(^{87}\mathrm{Rb}) = h \cdot 377.1074635(4)\ \mathrm{THz} \\ \Delta E_{D_1}(^{85}\mathrm{Rb}) = h \cdot 377.107385690(46)\ \mathrm{THz} \end{cases} \end{aligned} \tag{2}$$

for the two isotopes respectively. [1][2] Which implies that a laser wavelength of

$$\lambda = \frac{c}{\nu} = \frac{hc}{\Delta E} \approx 795\ \mathrm{nm} \tag{3}$$

is needed to resonantly excite the transition. Additionally, ^{87}Rb and ^{85}Rb have a nuclear spin of $I = 3/2$ and $I = 5/2$ respectively. The nuclear spin has a magnetic and electric quadrupolar moment, leading to the hyperfine splitting of the atomic energy levels. The contributions to the hyperfine splittings stem from the nuclear magnetic dipole moment in the magnetic field generated by the orbital motion of the valence electron at the position of the nucleus and the electrostatic interaction between the valence electron and the non-vanishing electric quadrupole moment of the nucleus. This leads to a coupling of the nuclear angular momentum $\vec{I}$ and the electron angular momentum $\vec{J}$ to the total angular momentum $\vec{F} = \vec{I} + \vec{J}$. Which allows us to characterize the hyperfine structure using the total angular momentum number F (for the full description of the fine and hyperfine structure of the D_1 transition of ^{87}Rb and ^{85}Rb see Appendix A.1). In the presence of a magnetic field B, the hyperfine levels split into sublevels depending on the angular distribution of the electron wave function due to the Zeeman effect. Furthermore the corresponding Zeeman splitting is given by

$$\begin{aligned} \Delta E &= g_F \mu_B m_F \mathrm{B} \\ (2) \rightsquigarrow \frac{\nu}{B} &= \frac{g_F \mu_B m_F}{h} \end{aligned} \tag{4}$$

where $g_F = g_F(F, I, J)$ is the Landé factor, μ_B the Bohr magneton and m_F the magnetic quantum number. Electric dipole transitions obey the following selection rules

$$\begin{aligned} \Delta F &= 0, \pm 1 \\ \Delta m_F &= 0, \pm 1 \end{aligned} \tag{5}$$

where $F = 0 \to F' = 0$ is not an allowed transition and the magnetic number depends on the polarization of the light.

To probe the internal energy structure of Rb atoms we are going to use absorption spectroscopy in this experiment. The basic idea is to illuminate a Rb vapor cell with a monochromatic laser beam of frequency ν_L and to then record the intensity of the transmitted light on a photodetector while tuning ν_L. Atoms at rest absorb light when the laser frequency coincides with an atomic transition i.e.

$$\nu_L \overset{!}{=} \nu_{i\to j} = \nu_0 \tag{6}$$

where $\nu_{i\to j}$ is the frequency of the transition from state i to state j. As a result, a sharp absorption line peak appears which is subject to line broadening due to the natural linewidth of the atomic transition

$$\begin{cases} \Gamma_{\mathrm{D}_1}(^{87}\mathrm{Rb}) = 2\pi \cdot 5.746(8)\ \mathrm{MHz} \\ \Gamma_{\mathrm{D}_1}(^{85}\mathrm{Rb}) = 2\pi \cdot 5.7500(56)\ \mathrm{MHz} \end{cases} \tag{7}$$

originating from the finite lifetime τ of the excited state over a time-energy uncertainty relation $\tau\Gamma \approx 1$. [1][2]

Since the atoms in the vapor cell have a finite temperature T, they follow a Maxwell-Boltzmann distribution centered around $v = 0$ and hence one needs to take the Doppler effect into account. In the frame of the atoms, the frequency of the laser is red-/blue shifted depending on the direction of travel of the atoms. The corresponding frequency change is

$$\delta\nu = \nu_0 \frac{v}{c} \tag{8}$$

where v is the velocity of the atom towards the laser. In order for the atom to absorb light resonantly, the laser frequency needs to be shifted by $-\delta\nu$. From Equation (8) and the fact that the atomic velocities follow a Maxwell-Boltzmann distribution we expect that the absorption profile has a frequency full-width at half-maximum (FWHM) amplitude of

$$\Delta\nu_{1/2} = \frac{\nu_0}{c}\sqrt{\frac{8k_BT\ln 2}{m}} \tag{9}$$

Furthermore, this causes a spread of observed frequencies, i.e., the absorption or emission line becomes broadened (more broadening at higher temperatures) and can be described by a Gauss function. This effect leads to the atomic hyperfine structure not being observable. Therefore a Doppler-free spectroscopy setup is required to resolve the hyperfine structure of the D_1 transition. In order to achieve this, two counterpropagating continuous-wave beams of the same frequency, probe and pump beam, are sent through the Rb vapor cell. The pump beam saturates the optical transition such that the probe beam then sees a transparent medium at frequency ν_0 and a Lamb dip turns up. The key idea is that only atoms with velocity $v = 0$ see both beams at the same frequency due to no doppler shift of the light. Hence Doppler-free spectroscopy does not work for atoms with non-zero velocity. For the case that $v \neq 0$ the frequencies of pump and probe beam differ in the atom's rest frame i.e. red-/blue shifted for opposite directions. Consequently these atoms cannot interact with both beams resonantly at the same time and therefore they will not contribute to the Lamb dip but only to the broadened background due to their velocity distribution. The resulting absorption profile for an atomic transition can then be modelled by a superposition of a Gaussian and a Lorentzian function

$$\begin{aligned} f(\nu) &= G(\nu) - L(\nu) + C \\ &= A_G \exp\left(-\frac{(\nu-\nu_0)^2}{2\sigma^2}\right) - A_L\frac{\gamma^2}{(\nu-\nu_0)^2+\gamma^2} + C \end{aligned} \tag{10}$$

where $G(\nu)$ is the Gaussian function and corresponds to the Doppler broadening, $L(\nu)$ is the Lorentzian function and corresponds to the Lamb dip. Additionally allowing to isolate each contribution to the absorption profile. From Equation 10 one can then extract the FWHM of each component, namely

$$\begin{aligned} \mathrm{FWHM}_G &= 2\sqrt{2\ln 2}\sigma \\ \mathrm{FWHM}_L &= 2\gamma \end{aligned} \tag{11}$$

which corresponds to the thermal Doppler broadening $\Delta\nu_{1/2}$ and the natural linewidth Γ of the atomic transition respectively.

For a multi-level atom additional peaks appear exactly midway between two atomic resonance peaks called cross-over resonances. They occur in Doppler-free saturated absorption spectroscopy. This happens when atoms with $v \neq 0$ are simultaneously resonant with two different transitions of a shared ground state due to opposite Doppler shifts from pump and probe beam. i.e.

$$\nu_x = \frac{1}{2}(\nu_{|g,e_1\rangle} + \nu_{|g,e_2\rangle}) \tag{12}$$

where ν_x is the cross-over resonance frequency and $\nu_{|g,e_1\rangle}$ and $\nu_{|g,e_2\rangle}$ are the resonant frequencies of the two transitions from a shared ground state $|g\rangle$ to different excited states $|e_1\rangle$ and $|e_2\rangle$.

In the interaction between a quantized atom and a classical light field we consider an atom with two different electronic states, a ground state $|g\rangle$ and an excited state $|e\rangle$ with orthonormal properties and energies $h\nu_g$ and $h\nu_e$ respectively. Which are the eigenstates of the atomic Hamiltonian $\mathcal{H}_0$ which can be written, using the completeness relation, as

$$\mathcal{H}_0 = h\nu_g |g\rangle\langle g| + h\nu_e |e\rangle\langle e|. \tag{13}$$

Applying an electric field induces an electric dipole. Hence the interaction Hamiltonian $\mathcal{H}_{int}$ can be writen as

$$\begin{aligned} \mathcal{H}_{int} &= q\hat{x}E(t) \\ &= q\hat{x}\varepsilon\cos\omega t. \end{aligned} \tag{14}$$

Expressing the position operator $\hat{x}$ in the two-level basis $\{|g\rangle, |e\rangle\}$ using the completeness relation we get

$$\begin{aligned} \hat{x} &= (|g\rangle\langle g| + |e\rangle\langle e|)\,\hat{x}\,(|g\rangle\langle g| + |e\rangle\langle e|) \\ &= |g\rangle\langle g|\,\hat{x}\,|e\rangle\langle e| + |e\rangle\langle e|\,\hat{x}\,|g\rangle\langle g| \\ &= |g\rangle\frac{\rho_{ge}}{q}\langle e| + |e\rangle\frac{\rho_{eg}}{q}\langle g| \\ &= |g\rangle\int d^3r\Psi_g^*(\vec{r})\,x\Psi_e^*(\vec{r})\langle e| \\ &\quad + |e\rangle\int d^3r\Psi_e^*(\vec{r})\,x\Psi_g^*(\vec{r})\langle g| \end{aligned} \tag{15}$$

where $\rho_{ge} = \rho_{eg}^*$ is the dipole matrix element of the electronic transition characterizing the strength of the electric dipole moment. Substituting Equation (15) into Equation (14) we get

$$\mathcal{H}_{int} = -\{\rho_{ge} |g\rangle \langle e| + \rho_{eg} |e\rangle \langle g|\} E(t) \tag{16}$$

which couples the ground state $|g\rangle$ to the excited state $|e\rangle$ i.e. $\langle e| \mathcal{H}_{int} |g\rangle \neq 0$. Therefore the full Hamiltonian of the atom in the presence of the electric field is given by

$$\mathcal{H} = \mathcal{H}_0 + \mathcal{H}_{int}. \tag{17}$$

as a superposition of Equations (13) and (16).

Using the existing framework one can establish a Λ-system consisting of two ground state levels $|g_1\rangle$, $|g_2\rangle$ and an excited state $|e\rangle$ and observe electromagnetically induced transparency (EIT).

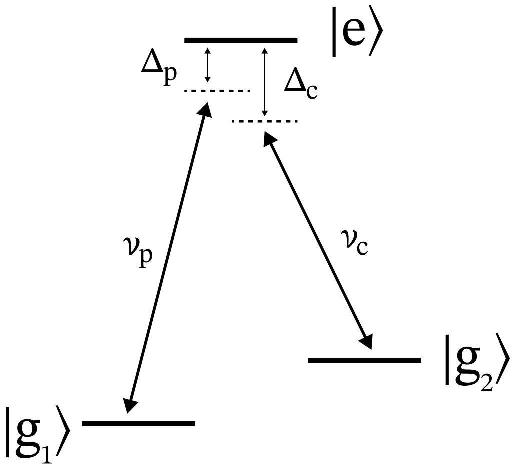

Fig. 1 | Schematic energy level diagram of the Λ-system. ν_p and ν_c are the laser frequencies of the probe and control beam respectively with the corresponding coupling of the transition from ground to excited state. Furthermore the each beam can have a non-zero detuning $\Delta_L = \nu_L - \nu_{i\to j}$ from the resonance $\nu_{i\to j} = \nu_i - \nu_j$.

Using a similar approach as above, the interaction Hamiltonian for the Λ-system can be written as

$$\mathcal{H}_{int,\Lambda} = \alpha_{e,g_1} |e\rangle \langle g_1| + \alpha_{e,g_2} |e\rangle \langle g_2| \tag{18}$$

where α_{e,g_1} and α_{e,g_2} are the interaction strengths induced by the light fields. Assuming resonant light fields, i.e. $\nu_L \overset{!}{=} \nu_{i\to j}$ and identical interaction strengths $|\alpha_{i\to j}|$, the quantum superposition state (dark state)

$$|\mathrm{DS}\rangle = \frac{1}{\sqrt{2}} (|g_1\rangle - |g_2\rangle) \tag{19}$$

is an eigenstate of the system and constant under time evolution. In contrast to the previous interaction Hamiltonian $\mathcal{H}_{int}$ from Equation (16), the interaction Hamiltonian of the Λ-system $\mathcal{H}_{int,\Lambda}$ does not couple the dark state $|\mathrm{DS}\rangle$ to the excited state $|e\rangle$, i.e. $\langle e| \mathcal{H}_{int,\Lambda} |\mathrm{DS}\rangle = 0$. At the two-photon resonance condition i.e. $\Delta_p = \Delta_c$ a narrow transmission peak (EIT window/medium becomes transparent) appears whose position can be tuned via the magnetic field making use of the Zeeman effect. The state $|\mathrm{DS}\rangle$ is hence a quantum superposition of the two ground states. The two excitation amplitudes of the excited state cancel eachother resulting in a vanishing population of the excited state by destructive interference. Furthermore the dark state cannot decay into other states and is therefore unaffected by its environment hence the name.

The following figure shows the specific cases of Λ-type configurations for the ^{87}Rb $5^2\mathrm{S}_{1/2}(\mathrm{F}=2) \to 5^2\mathrm{P}_{1/2}(\mathrm{F}'=1)$ transition.

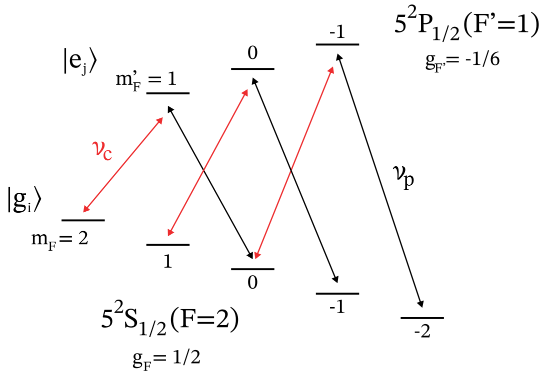

Fig. 2 | Schematic energy level of the Λ-system for the ^{87}Rb $5^2\mathrm{S}_{1/2}(\mathrm{F}=2) \to 5^2\mathrm{P}_{1/2}(\mathrm{F}'=1)$ transition. F denotes the total angular momentum quantum number and the hyperfine state Zeeman sublevels are denoted by m_F for the ground states $|g_i\rangle$ and $m_{F'}$ for the excited states $|e_j\rangle$. Furthermore, the probe and control laser frequencies ν_p and ν_c, with polarizations σ^- and σ^+ respectively, are shown with the corresponding dipole-allowed transitions according to the selection rules defined in Equation (5). Additionally the Landé $g_F/g_{F'}$-factors for the ground and excited states are indicated. [1]

An external magnetic field B splits the Zeeman sublevels of each hyperfine state due to the Zeeman effect according to Equation (4). This lifts the degeneracy of the ground state Zeeman levels and makes the two ground states have different energies creating a resolvable two-photon resonance condition for the EIT essential for tuning the probe and control beam such that the frequency difference matches the energy splitting between the two ground states. [3]

METHODS

The main purpose of this experiment is to observe an EIT signal in the ^{87}Rb atomic system. However, in this experiment a rubidium vapor cell is used which contains both isotopes. In order to measure the desired EIT signal a spectroscopy setup is used to ensure that the laser frequency ν_L is resonant with the ^{87}Rb $5^2\mathrm{S}_{1/2}(\mathrm{F}=2) \to 5^2\mathrm{P}_{1/2}(\mathrm{F}'=1)$ transition. Thus the experimental setup consists of two parts namely a spectroscopy and EIT part on the same optical table sharing some components (see Appendix A.3 for the full setup).

In this experiment a distributed feedback (DFB) laser with a wavelength of $\lambda = 795 \pm 0.5$nm is used with intent to resonantly excite the D_1 transition of rubidium according to Equation (3). The frequency of the DFB laser light is dependent on the applied current, supplied by a current control unit, and temperature, regulated via a Peltier thermoelectric element, and has a linewidth of some MHzs. Furthermore we periodically modulate the frequency of the laser beam by applying an additional changing input signal to an additional (AF) input in addition to the constant current of the laser driver in the control unit. This allows us to scan the frequency of the laser periodically and to observe the resonant absorption when hitting an atomic resonance frequency of Rb. An additional electronic box, lock box, allows tuning the amplitude and offset of the signal which is directly applied to the AF input of the laser diode current control.

Furthermore to reach the desired experimental conditions, optical instruments such as optical insulators, lenses, mirrors, neutral density (ND) filters, polarizing beam splitters and waveplates are used to manipulate the laser beam.

A general explanation of the effect of optical elements on the laser beam i.e. the electromagnetic field wave can be achieved using Jones calculus. W.l.o.g. we start with a monochromatic plane electromagnetic wave propagating in the z-direction:

$$\begin{aligned}\vec{E}(z,t) &= re\{\vec{E}_0 e^{i(kz-\omega t)}\} \\ &= re\{\begin{pmatrix} E_{0,x}e^{i\phi_x} \\ E_{0,y}e^{i\phi_y}\end{pmatrix} e^{i(kz-\omega t)}\} \\ &\overset{\delta:=\phi_y-\phi_x}{=} re\{\begin{pmatrix} E_{0,x} \\ E_{0,y}e^{i\delta}\end{pmatrix} e^{i(kz-\omega t)}\} \\ &= re\{\vec{J}e^{i(kz-\omega t)}\}\end{aligned} \tag{20}$$

where $\vec{E}_0$ is the amplitude vector, $k = \frac{2\pi}{\lambda}$ the wave number, $\omega = 2\pi\nu$ the angular frequency, ϕ the phase and $\vec{J}$ the Jones vector describing the polarization state in the xy-plane which can be normalized. The Jones vector $\vec{J}$ can be transformed by a linear optical element, e.g. a polarizer, waveplate or beam splitter, which can be described by the a 2×2 matrix $\mathcal{M}$, the Jones matrix. Hence the effect of the optical element on the Jones vector or electromagnetic field wave can be written as the product of the input Jones vector $\vec{J}_{in}$ and the matrix $\mathcal{M}_i$ of the optical element especially since we are working with monochromatic light and are only interested in relative phase shifts in the following way:

$$\vec{J}_{out} = \prod_i \mathcal{M}_i \vec{J}_{in} \tag{21}$$

In this formalism leaving out global phase factors (no effect on the polarization state) $\lambda/2$-waveplates which shift the polarization direction of linearly polarized light (e.g. horizontally/vertically linear polarization: $(1,0)^{\mathrm{T}} := |H\rangle$ / $(0,1)^{\mathrm{T}} := |V\rangle$) and $\lambda/4$-waveplates which convert linearly polarized light into circularly polarized light (e.g. right circular polarization σ^+: $\frac{1}{\sqrt{2}}(1,-i)^{\mathrm{T}} := |R\rangle = \frac{1}{\sqrt{2}}(|H\rangle - i\,|V\rangle)$) and vice versa can be modelled in the following way:

$$\begin{aligned}\mathcal{M}_{\lambda/2}^{(\text{x-fast})} &= \begin{pmatrix} 1 & 0 \\ 0 & -1 \end{pmatrix} \\ \mathcal{M}_{\lambda/4}^{(\text{x-fast})} &= \begin{pmatrix} 1 & 0 \\ 0 & i \end{pmatrix}\end{aligned} \tag{22}$$

where in this case the fast axis of the waveplate is aligned with the x-axis as indicated. This could be extended to the case of arbitrarily rotated elements by using rotation matrices etc. but should suffice to explain the effect of waveplates and optical isolators. The latter is used to prevent back reflections into the laser diode which could potentially disturb its operation. An isolator consists of two polarizers describable by Jones matrices and a Faraday rotator in between which rotates the polarization direction of the light by 45° using the Faraday effect. As a result the light can only pass through the isolator in one direction. A polarizing beam splitter (PBS) splits the beam into two differrent spatial paths i.e. a transmitted and reflected beam of orthogonal linear polarizations depending on the polarization state. In this setup horizontally polarized light will be transmitted. This is outside the standard Jones calculus scope but can nevertheless be described by modelling the effect on each output beam seperately, each with its own jones matrix applied to the input vector. Therefore the Jones matrix of the PBS can be written as

$$\begin{aligned}\mathcal{M}_{PBS,T} &= \begin{pmatrix} 1 & 0 \\ 0 & 0 \end{pmatrix} \\ \mathcal{M}_{PBS,R} &= \begin{pmatrix} 0 & 0 \\ 0 & 1 \end{pmatrix}\end{aligned} \tag{23}$$

where the first matrix describes the transmitted beam and the second matrix describes the reflected beam assuming ideal behavior.

Additionally, the setup contains two acousto-optical modulators (AOMs). AOMs make use of the acousto-optical effect, which is the interaction between an acoustic wave and an electromagnetic wave in a medium. In this experiment, the AOM driving frequency ν_{RF} is set at about 80MHz by external application of a radio-frequency voltage signal generated by a voltage-controlled oscillator (VCO). The output frequency of the VCO can be tuned by applying a control voltage $\in [0, 15]$ V. Furthermore the RF signal is amplified before being sent to the AOM, its frequency is monitored using a frequency counter. After the AOMs, the laser beam is distributed over different diffraction orders, where the 1^{st} order beam was scattered once and has the angular frequency $\omega_L + \omega_{\mathrm{RF}} = \omega_L + 2\pi\nu_{\mathrm{RF}}$. For the EIT part, control and probe beams pass twice through individual AOMs, which shift the frequencies of the beams. The probe beam requires that $\nu_{\mathrm{RF,probe}}$ is periodically varying so that its optical frequency is scanned over time. Whereas the control beam is set to a fixed frequency $\nu_{\mathrm{RF,control}}$, in order to observe the two-photon resonance condition in EIT. Since probe and control beam originate from two different AOMs the relative frequency between them is given by

$$\nu_{\mathrm{probe}} - \nu_{\mathrm{control}} = 2\left(\nu_{\mathrm{RF,probe}} - \nu_{\mathrm{RF,control}}\right). \tag{24}$$

The central part of the EIT setup creates the so-called science chamber, which contains a rubidium vapor cell surrounded by a heating element and a solenoid in order to produce the homogeneous magnetic field needed for lifting the degeneracy between the different Zeeman levels and observing EIT. Additionally, the science chamber is shielded from other external magnetic field sources by four layers of mu-metal material. The magnetic field inside the solenoid can then be approximated by

$$\mathrm{B} = \frac{\mu_0 \mathrm{N} I}{L} \tag{25}$$

where N = 130 is the number of windings, $L = 16\text{cm}$ is the length of the solenoid, μ_0 is the vacuum permeability and I the current through the solenoid.

Finally, all laser beam intensities are detected using photodiodes which are calibrated to measure 5V/mW and saturates about 9V. To prevent oversaturation of the photodiode, ND-filters are used to reduce the intensity of the laser beam. Therefore the power measured by the photodiode for different laser currents is given by

$$P(I) = P(V(I), F_{\text{ND}}) = \frac{V(I)}{5} \cdot 10^{F_{\text{ND}}} \tag{26}$$

where V is the voltage measured by the photodiode and F_{ND} is the neutral density filter factor.

The specific procedure of the experiment is as follows: After the laser passes through beam-shaping optics and an optical isolator, the experimental procedure begins with characterizing the laser beam using a photodiode and a ND-filter.

The beam is then split into control and probe using a combination of a $\lambda/2$-waveplate and a PBS, with an additional optical isolator placed between the first beamsplitter and the second waveplate.

Next, the VCO is calibrated. AOMs are then set up by identifying and optimizing the first diffraction order using pinholes. For the control beam, a retroreflecting mirror and a $\lambda/4$ waveplate are aligned so that the first-order diffracted beam is reflected back into the AOM, and the waveplate is adjusted such that the reflected beam is transmitted through the PBS. The probe beam setup follows a similar configuration, but due to frequency-dependent diffraction angles caused by the non-constant RF frequency $\nu_{\text{RF,probe}}$ driving the probe AOM, a cat-eye configuration including a lens is added to stabilize the beam alignment. [4]

A portion of the control beam is then split off using a beamsplitter and repurposed for rubidium spectroscopy. This portion is divided into a probe and pump beam using another beamsplitter; the probe passes through an ND-filter and the rubidium vapor cell before reaching a photodiode, while the pump is directed onto a retroreflecting mirror to produce a counterpropagating beam, enabling Doppler-free spectroscopy. Doppler-free absorption lines are observed by scanning the laser frequency using the lockbox and monitoring the transmitted probe intensity on the photodiode.

Returning to the EIT configuration, the control and probe beams are superimposed using a PBS and directed into the science chamber, making sure that the probe beam is about 10 times weaker than the control beam. Two $\lambda/4$-waveplates and a PBS are used to generate orthogonal circularly polarized fields and to separate the beams after they pass through the chamber, ensuring that only the probe beam reaches the photodiode. The laser frequency is then fixed near an absorption line in the rubidium spectrum using the lockbox. A sawtooth waveform of approximately 100Hz in the voltage range of 6-10 V is generated and applied to the probe VCO, thereby modulating the probe beam frequency around that of the control.

Finally, the EIT signal is observed by heating the science chamber and applying a current to the solenoid to generate a homogeneous magnetic field, with the signal monitored as a function of frequency detuning between probe and control. [3]

DATA ANALYSIS AND RESULTS

If not mentioned otherwise, the uncertainties of the values are calculated using Gaussian error propagation. (see Appendix A.2).

The laser output power $P(I)$ and threshold current $I_{th.}$ was calculated using Equation (26). The ND-filter factor that was used is $F_{\text{ND}} = 2.0$ with an error of $\sigma_{F_{\text{ND, 633nm}}} = 0.1$ at 633nm. [5] Since the laser has a wavelength of $\lambda = 795 \pm 0.5\text{nm}$, an error of $\sigma_{F_{\text{ND, 795nm}}} = 0.13$ i.e. 30% higher than the literature value was used as a rough estimate. Then by performing a linear fit to the data points, in the following figure, the laser output power was determined to be $P(I) = (520 \pm 30)\frac{\text{mW}}{\text{mA}} I - (27 \pm 2)\text{mW}$ with a threshold current of $I_{th.} = 0.052 \pm 0.005\text{mA}$.

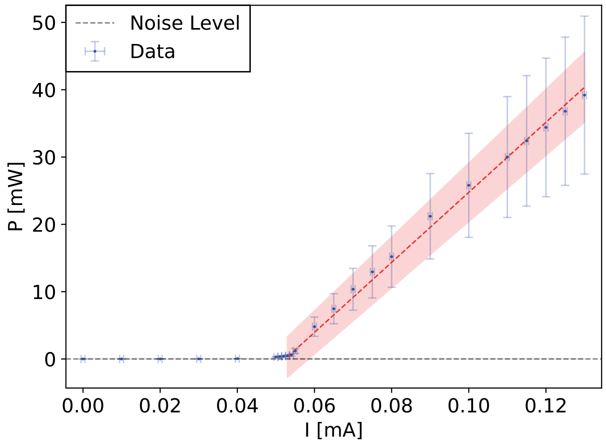

Fig. 3 | Laser power P as a function of the laser current I with corresponding errors. The red dotted line is the linear fit that was performed where the red area marks the error of the fit. Furthermore, the noise level is indicated by the black dotted line.

Setting up the Doppler-free spectroscopy allowed us to obtain the absorption spectrum of the rubidium gas, displayed in the following figure.

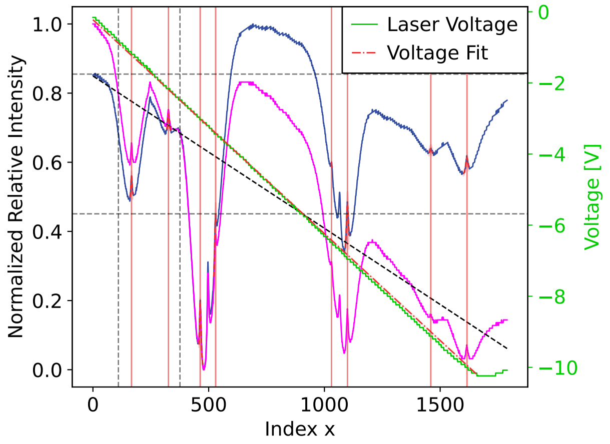

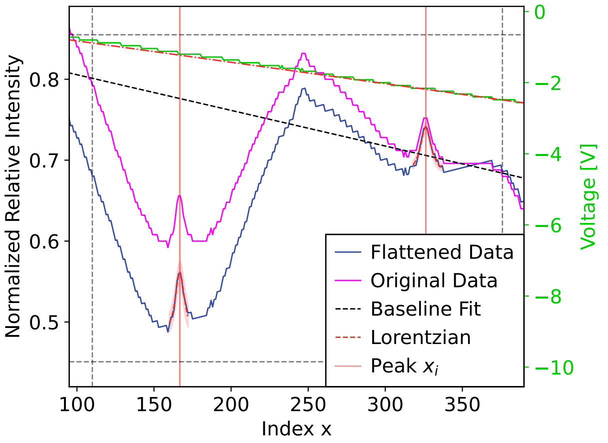

Fig. 4 | The absorption spectrum of rubidium gas in purple is displayed as normalized relative intensity detected on the photodiode as a function of the index x of the datapoint in the saved data from the digital storage oscilloscope (DSO). Furthermore the laser voltage is displayed in green on a secondary y-axis, also as a function of the index. Additionally, a linear fit was performed to the laser voltage displayed as a red dash-dotted line. Since the laser power/voltage is directly related to the frequency ν_L there is this decline in intensity detected at the photodiode. Therefore a baseline fit, displayed as a black dotted line, was performed to account for this effect and the data was flattened and displayed in blue which will increase the precision of identifying transition frequencies in the spectrum. To identify the transition frequencies, a Lorentzian fit $L(\nu)$ according to Equation (10) was applied in a local region around each peak. The fit as well as the from the fit parameters extracted peak position is displayed in a red dotted line with the corresponding error displayed in a red shaded area. Furthermore, the lower plot displays a zoomed-in view of the dataset and performed methods marked by the gray dotted window.

The peaks that were identified at this point still do not carry any physical meaning, since it is merely an index of the data point in the saved data from the DSO. In order to assign frequencies to the peaks, literature values of the ^{87}Rb- and ^{85}Rb D$_1$ transition frequencies displayed in the following table were used.

Table 1 | Literature values for the ^{87}Rb- and ^{85}Rb D$_1$ transition frequencies in ascending order. [1][2]

Isotope	Transition Frequency [THz]
^{87}Rb	377.1043901(4)
	377.1052067(4)
^{85}Rb	377.1059099(1)
	377.10627146(8)
	377.1089456(1)
	377.10930719(8)
^{87}Rb	377.1112248(4)
	377.1120414(4)

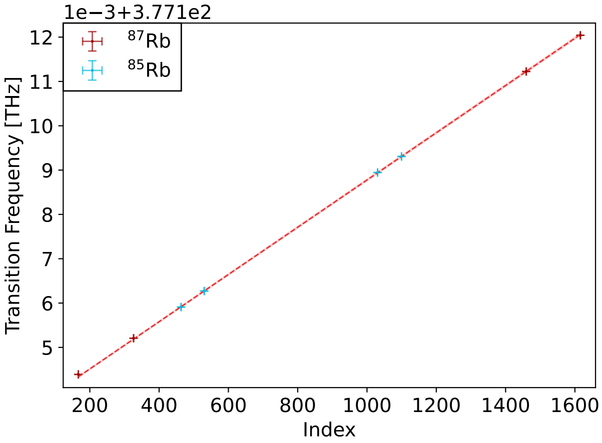

Fig. 5 | Transformation of the index to frequency. The transition frequency of each isotope of the D$_1$ line from Table 1 was plotted as a function of the estimated peak position of the transition. Then a linear fit over all found transition peaks which were assigned with the corresponding literature value was performed to calibrate the whole spectrum displayed.

The advantage of this method is that the conversion from index to frequency is performed on a uniformly spaced dataset so it does not require interpolation or an additional dataset. A disadvantage is that after this conversion it requires that the spectrum is exactly calibrated to only one window of the spectrum i.e. no zooming in on specific parts which would allow a higher precision if needed. Therefore, we convert the index to voltage to frequency, shown in the following figure, which allows us to zoom in on specific parts of the spectrum and still have a calibrated spectrum.

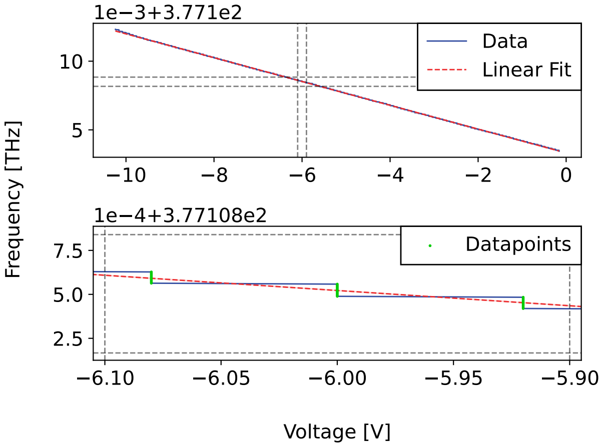

Fig. 6 | Frequency displayed as a function of laser voltage. The lower plot shows a zoomed in view of the datapoints measured by the DSO. Since the sampling rate is finite this requires us to either interpolate the data or perform a linear fit in order to retain as most information as possible and display a continuous frequency axis which carries an additional error. By performing a linear fit the frequency as a function of voltage was found to be $f(U) = -0.0008668(2)\frac{\mathrm{THz}}{\mathrm{V}}\mathrm{U} + 377.103321(1)\mathrm{THz}$

After calibration using Figure 5 and Figure 6 we now have the calculated transition frequencies as well as cross-over frequencies and can display them in a physically meaningful way.

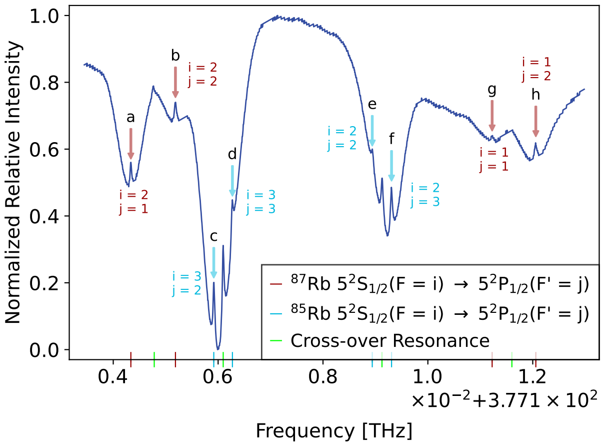

Fig. 7 | Rubidium absorption spectrum displayed as normalized relative intensity as a function of frequency. Furthermore, the peaks have been labeled with their corresponding transition for each isotope seperately. Additionally, the cross-over resonances were estimated using a Lorentzian fit and marked in green on the x-axis.

Using the terminology from Figure 7, the following tables summarize the transition frequencies and splittings of the ^{87}Rb- and ^{85}Rb D$_1$ line as well as the cross-over resonances.

Table 2 | Literature and experimentally obtained frequencies in THz using the above mentioned methods for the ^{87}Rb- and ^{85}Rb D$_1$ transitions as well as theoretical predictions for the cross-over-resonances using Equation (12) displayed in ascending order. [1][2][3]

Transition $i \rightarrow j$	Determined	Literature
a	377.104336(9)	377.1043901(4)
b	377.10519(1)	377.1052067(4)
c	377.10592(1)	377.1059099(1)
d	377.10627(1)	377.10627146(8)
e	377.10894(1)	377.1089456(1)
f	377.10931(1)	377.10930719(8)
g	377.11123(2)	377.1112248(4)
h	377.11206(2)	377.1120414(4)

Cross-over Resonance ν_x	Determined	Th. Prediction
a, b	377.104782(9)	377.104761(7)
c, d	377.106097(9)	377.106095(7)
e, f	377.109125(9)	377.10912(1)
g, h	377.111602(9)	377.11164(1)

Furthermore, the splittings between the transitions were calculated using the determined transition frequencies and are displayed in the following table.

Table 3 | Literature and experimentally obtained state splittings for the ^{87}Rb- and ^{85}Rb D$_1$ transitions. [1][2][3]

Isotope	Splitting	Determined	Literature
^{87}Rb	b − a	850(10)MHz	816.656(30)MHz
	h − g	830(30)MHz	816.656(30)MHz
	g − a	6.89(2)GHz	6.83468261090429(9)GHz
	h − b	6.87(2)GHz	6.83468261090429(9)GHz
^{85}Rb	d − c	360(20)MHz	361.58(17)MHz
	f − e	370(20)MHz	361.58(17)MHz
	e − c	3.02(2)GHz	3.0357324390(6)GHz
	f − d	3.03(2)GHz	3.0357324390(6)GHz

In a final step of the spectroscopy part, the ^{87}Rb $5^2S_{1/2}(F = 2) \rightarrow 5^2P_{1/2}(F' = 1)$ transition was selected due to its prominence in the spectrum to extract the thermal broadening from a Gaussian fit. Using the estimated fit parameters from Equation (10) and the Equation (11) to calculate the FWHM of the Gaussian fit, the thermal broadening was determined to be $\Delta\nu_{1/2,calc.}(T = 330 \pm 10\text{K}) = 0.549 \pm 0.002\text{GHz}$. Whereas the theory predicts a thermal broadening of $\Delta\nu_{1/2,th.}(T = 330 \pm 10\text{K}) = 0.529 \pm 0.008\text{GHz}$ using Equation (9). Furthermore, since the absorption profile was successfully fitted as displayed in the following figure, the linewidth of the transition was extracted as well. The linewidth was determined to be $\Gamma_{calc.} = 2\pi \times 7.0 \pm 0.5\text{MHz}$, with the literature value being $\Gamma_{lit.} = 2\pi \times 5.746 \pm 0.008\text{MHz}$ from Equation (7).

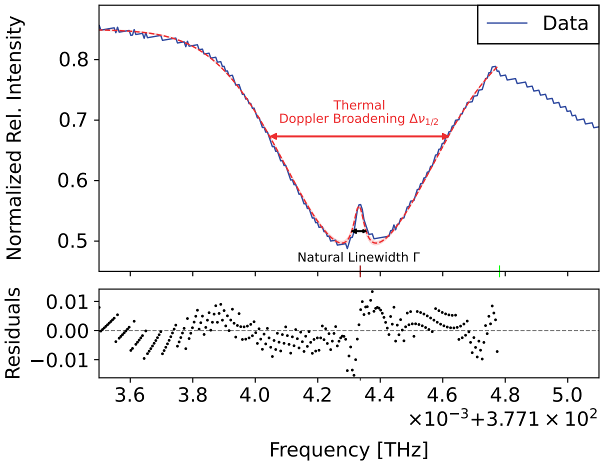

Fig. 8 | The absorption profile zoomed in on the ^{87}Rb $5^2S_{1/2}(F = 2) \rightarrow 5^2P_{1/2}(F' = 1)$ transition. The fitted profile is a superposition of a Lorentzian and a Gaussian function as in Equation (10), capturing both the natural linewidth and the Doppler broadening effects of the transition, shown as the red dotted line with the corresponding error as a shaded area. Furthermore, the FWHM of the Gaussian i.e. Doppler broadening $\Delta\nu_{1/2}$ and the FWHM of the Lorentzian i.e. linewidth Γ of the transition are displayed in the plot. Additionally, the residuals of the fit are shown in the lower plot, where the dashed line indicates the zero level.

After the spectroscopy part was completed such that the laser frequency was calibrated to the ^{87}Rb $5^2S_{1/2}(F = 2) \rightarrow 5^2P_{1/2}(F' = 1)$ transition, the EIT part of the experiment was performed. Since in this part the AOMs and their detuning are fundamental to the experiment, the AOMs were characterized first shown in the following figure.

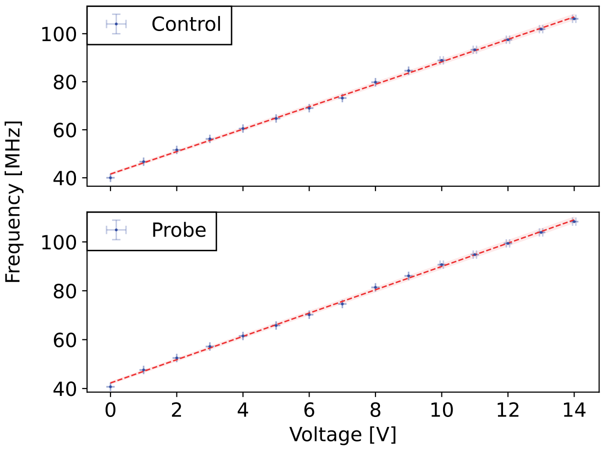

Fig. 9 | Characterization of the control and probe beam AOMs. The control and probe beam frequency are plotted as a function of the voltage applied to the AOMs. Furthermore, for each a linear fit was performed indicated by a red dotted line with the corresponding error shaded in red. Thus, for the control beam AOM we have $\nu_{\text{control}}(U) = (4.67 \pm 0.05)\frac{\text{MHz}}{\text{V}}U + (41.6 \pm 0.4)\text{MHz}$ and for the probe beam AOM $\nu_{\text{probe}}(U) = (4.77 \pm 0.05)\frac{\text{MHz}}{\text{V}}U + (42.3 \pm 0.4)\text{MHz}$.

In the last part the EIT signal was measured by scanning the probe beam frequency around the control beam frequency. Furthermore, by applying different currents to the solenoid, the magnetic field was varied according to Equation (25) and the EIT signal was measured for different magnetic field strengths for a current range $\in [-0.4, 0.45]\text{mA}$. One such measurement is displayed in the following figure.

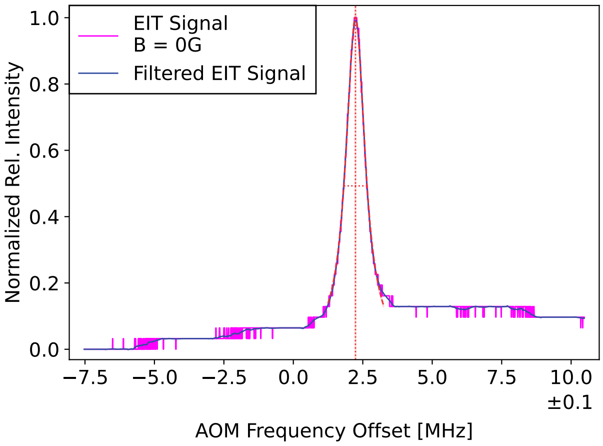

Fig. 10 | Normalized relative EIT signal intensity displayed as a function of the AOM frequency offset i.e. detuning of probe and control beams for a magnetic field strength of 0G or no current to the solenoid, with the x-axis conversion error displayed in the bottom right corner. Since the signal was relatively weak, there is a lot of additional noise in the signal. Therefore, before any data analysis was performed, the data was smoothed using a Savitzky-Golay filter, where the filtered EIT signal is displayed in blue. Afterwards, the EIT signal peak was fitted using a Lorentzian function displayed as a dotted red line with the corresponding error shaded in red. Additionally from the fit parameters the FWHM as well as the peak position of the EIT signal were extracted.

This procedure was repeated for different magnetic field strengths, where the EIT signal was measured and the peak position and FWHM were extracted (see Appendix A.4 for all measured EIT signals). This process posed many challenges, particularly in distinguishing the EIT signal from the background noise and ensuring the accuracy of the Lorentzian fits which was not always successfully achieved. The findings of the EIT signal peak positions and FWHM for different magnetic field strengths are summarized in the following figure.

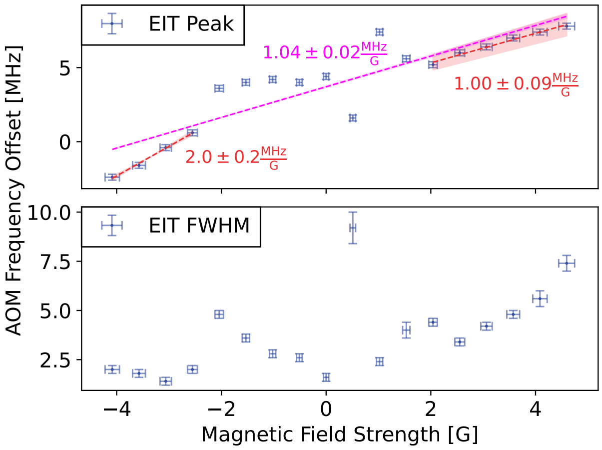

Fig. 11 | The upper plot displays the EIT signal peak positions as detuning of the probe beam from the control beam for different magnetic field strengths. Furthermore, a linear fit was performed once for all the data points, displayed as a purple dotted line with the error as shaded area, and then for the regions with an absolute field strength of ≥ 2G displayed as red dotted lines and the corresponding error of the fit shaded in red. The slopes of each region are indicated in the plot. The datapoints beyond 2G were chosen for the reason that they show a linear dependence and also do not fluctuate as much as the datapoints below 2G due to instability of estimating the fit parameters for the peak position i.e. Lorentzian fit. Therefore by leaving out the datapoints below 2G and taking the average of the slopes of the two linear fits, the average slope was determined to be $a = 1.5 \pm 0.5\frac{\text{MHz}}{\text{G}}$. The lower plot shows the corresponding FWHM values extracted from the Lorentzian fits. These results provide insight into the behavior of the EIT signal under varying magnetic field conditions.

After estimating the slope of the EIT peak position as a function of the magnetic field strength which was found to be $a = 1.5 \pm 0.5\frac{\text{MHz}}{\text{G}}$, we can compare it to the theoretical prediction using the Zeeman splitting formula from Equation (4). Since in the observed transition we have $g_F = \frac{1}{2}$ and $m_F = 2$, we can rewrite the equation as

$$\frac{\nu}{B} = \frac{\mu_B}{h} = 1.399624624(56)\frac{\text{MHz}}{\text{G}} \tag{27}$$

where μ_B is the Bohr magneton and h is Planck's constant. [1]

Discussion of Results

The results of the experiment demonstrate successful implementation of both Doppler-free atomic spectroscopy and

EIT in rubidium. The spectroscopy setup enabled resolution of the hyperfine transitions of both ^{87}Rb and ^{85}Rb isotopes for the $5^2\mathrm{S}_{1/2} \rightarrow 5^2\mathrm{P}_{1/2}$ or D_1 transition.

As the values in Table 2 indicate, the used frequency calibration method was accurate such that 6 out of 8 obtained transition frequencies coincide with the literature values. Where the two frequencies that are not within the uncertainty of literature values are the ^{87}Rb $5^2\mathrm{S}_{1/2}(F = 2) \rightarrow 5^2\mathrm{P}_{1/2}(F' = 1)$ transition and the $5^2\mathrm{S}_{1/2}(F = 2) \rightarrow 5^2\mathrm{P}_{1/2}(F' = 2)$ transition which only differs by a few MHz. One has to take into account that the calibration was carried out by using exactly these 8 literature values by performing a linear fit to them and the estimated peak positions. Therefore, a possible source of error could be in performing the linear fit itself which was estimated to be too small or in estimating the peak positions in the spectrum using Lorentzian fits. Before carrying out the fits, the dataset was flattened for a more accurate identification of the peaks but the error of this procedure was not taken into account. In addition, no error analysis on the laser itself i.e. quantifying the laser linewidth which is in the range of a few MHz was performed. Merely the laser power was calibrated using the photodiode and the ND-filter, where the uncertainty was estimated without thorough justification by simply choosing a larger value than the literature value because of different wavelengths. Hence, the uncertainty of the transition frequencies is likely underestimated.

For the cross-over resonance frequency, the theoretical prediction coincides only with the cross-over resonance frequency for the "c, d" transitions. However the "a, b" and "e, f" cross-over resonance frequencies differ only by a few MHz, whereas the "g, h" cross-over resonance frequency is off by a larger margin. This is likely the effect of already mentioned uncertainties in estimating the transition frequencies which translates into the observed discrepancies.

The state splittings in Table 3 show that for the ^{85}Rb D_1 line all experimentally obtained values lie within the uncertainty of the literature values. For the ^{87}Rb D_1 line, only the $h - g$ splitting is within the uncertainty of the literature value, whereas all the other values differ by a few MHz as mentioned in the previous spectroscopy measurements.

Lastly the thermal broadening and linewidth of the ^{87}Rb $5^2\mathrm{S}_{1/2}(F = 2) \rightarrow 5^2\mathrm{P}_{1/2}(F' = 1)$ transition does not lie within the uncertainty of the theoretical prediction nor literature value but once again only differs by a few MHz. Furthermore for the thermal broadening, a relatively large temperature uncertainty was chosen since neither the temperature nor the pressure inside the rubidium vapor cell were monitored at all times during the experiment. And hence no error analysis was performed on the rubidium vapor cell in general. The natural linewidth was determined using the FWHM of the Lorentzian fit to the absorption profile. It is likely that the superposition of Gaussian and Lorentzian profiles might not account for all effects that contribute to the linewidth of the transition and hence the uncertainty is likely underestimated since the model is underdescriptive.

The EIT measurements support the quantum interference model. A clear EIT peak was observed for zero magnetic field and varied consistently under applied magnetic fields as Figure 10 and Figure 11 suggest. The dependence of the EIT peak position on the magnetic field strength confirms the role of Zeeman splitting in tuning the two-photon resonance condition. Furthermore, the experimentally obtained Zeeman splitting of the EIT signal lies within the uncertainty of the theoretical prediction using the Zeeman splitting formula from Equation (4). However, the EIT signal was weak and noisy, making it challenging to extract precise values for the peak position and FWHM to carry out a scientifically based quantification of this phenomenon. Furthermore since the EIT signal was noisy, an additional filtering was applied to the data before fitting the EIT signal peak where neither the error nor the method of filtering was thoroughly characterized or justified besides keeping the overall shape of the signal intact. On top of that, in the experimental realization the beams might not have been perfectly overlapped or the magnetic fields were not perfectly homogenous in space leading to a spatially dependent energy splitting between the states which is clearly visible in the data. Nevertheless, the general trend matches the theoretical expectation i.e. EIT peak appearance, magnetic field dependent shift and expected symmetry supporting the dark state formation.

CONCLUSION

In this experiment we successfully implemented Doppler-free atomic spectroscopy and observed electromagnetically induced transparency (EIT) in natural rubidium. By calibrating the laser frequency using literature values for the D_1 line of rubidium, we resolved the hyperfine structure of both ^{87}Rb and ^{85}Rb with high precision. The experimentally obtained values generally agreed well with literature values and theoretical predictions, with some discrepancies likely due to uncertainties in the experimental setup and data analysis methods, namely limitations in peak detection and error estimation.

Furthermore, the EIT signal was clearly observed, and shown to depend on the applied magnetic field, consistent with theoretical expectations based on Zeeman splitting and the two-photon resonance in a Λ-system providing experimental verification of the coherent atom-photon interaction in a three-level system. However, the EIT signal was weak and noisy, likely due to experimental imperfections.

The discrepancies from the literature values and theoretical predictions are expected to be a consequence of systematic errors included in the experiment setup, and underdescriptive models used to the describe the behavior of the system especially in peak detection and FWHM estimation. Furthermore, no extensive error analysis has been performed on the experimental setup such as the laser linewidth, the purity of rubidium, the homogenity of the magnetic field or the temperature and pressure inside the vapor cell. Additionally, the laser light might not have been perfectly circularly polarized or always perpendicularly aligned resulting in imperfect polarizations. Also, no error analysis was performed on the linear optical elements such as the mirrors, PBS and its extinction ratio, waveplates or lenses. These factors could have contributed to the observed discrepancies in the results.

To improve the experiment, one should perform an extensive error analysis and characterization of the experimental setup to remove or characterize additional noise present in the signal. Also, the temperature and pressure inside the rubidium vapor cell should be monitored and controlled to ensure a stable environment. As well as ensuring optimal alignment of the laser beams and their polarizations to minimize systematic errors. Additionally, a more robust method for peak detection and fitting could be implemented.

Acknowledgments

The execution of the experiment in the laboratory was supported in part by Julian Stumpf[1] and Dr.Zijie Zhu[2].

References

1. Steck, D. A. *Rubidium 87 D Line Data* `https://steck.us/alkalidata/rubidium87numbers.1.6.pdf`. Revision 1.6, 14 October 2003. Last accessed: 26 May 2025. Los Alamos, NM 87545, USA, Oct. 2003.
2. Steck, D. A. *Rubidium 85 D Line Data* `http://steck.us/alkalidata`. Revision 2.3.3, 28 May 2024. Copyright © 2008 by Daniel Adam Steck. Distributed under the Open Publication License v1.0 or later. Last accessed: 26 May 2025. 1274 University of Oregon, Eugene, OR 97403-1274, USA, May 2024.
3. Mottl, R. *ASL: Atom-Photon Interaction Experiment* `https://vp.phys.ethz.ch/Experimente/pdf/ASL_atom_photon_interaction.pdf`. Version 1.1. Accessed: 2025-04-28. Oct. 2014.
4. Donley, E. A., Heavner, T. P., Levi, F., Tataw, M. O. & Jefferts, S. R. Double-pass acousto-optic modulator system. *Review of Scientific Instruments* **76,** 063112 (2005).
5. Thorlabs, Inc. *NE20A Ø25 mm Absorptive Neutral Density Filter, SM1-Threaded Mount, Optical Density: 2.0* `https://www.thorlabs.com/thorproduct.cfm?partnumber=NE20A`. AutoCAD PDF drawing available under the "Drawings and Documents" section. 2000. (2025).

---

[1] jstumpf@ethz.ch

[2] zhuzi@ethz.ch

A Appendix

A.1 Fine and Hyperfine Structure of the D_1 Transition

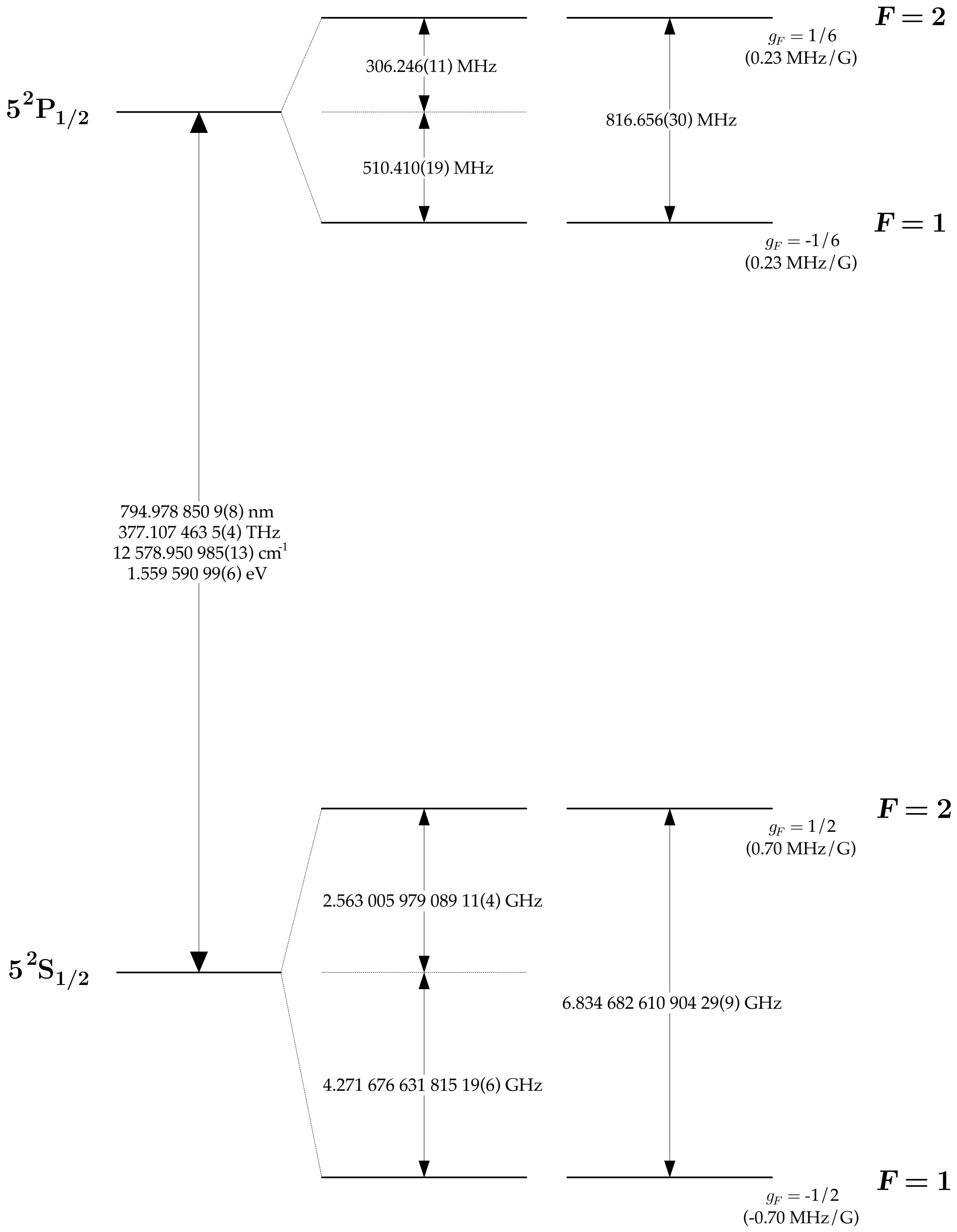

Fig. A.1.1 | ^{87}Rb D_1 transition hyperfine structure, with frequency splittings between the hyperfine energy levels. The approximate Landé g_F-factors for each level are also given, with the corresponding Zeeman splittings between adjacent magnetic sublevels. [1]

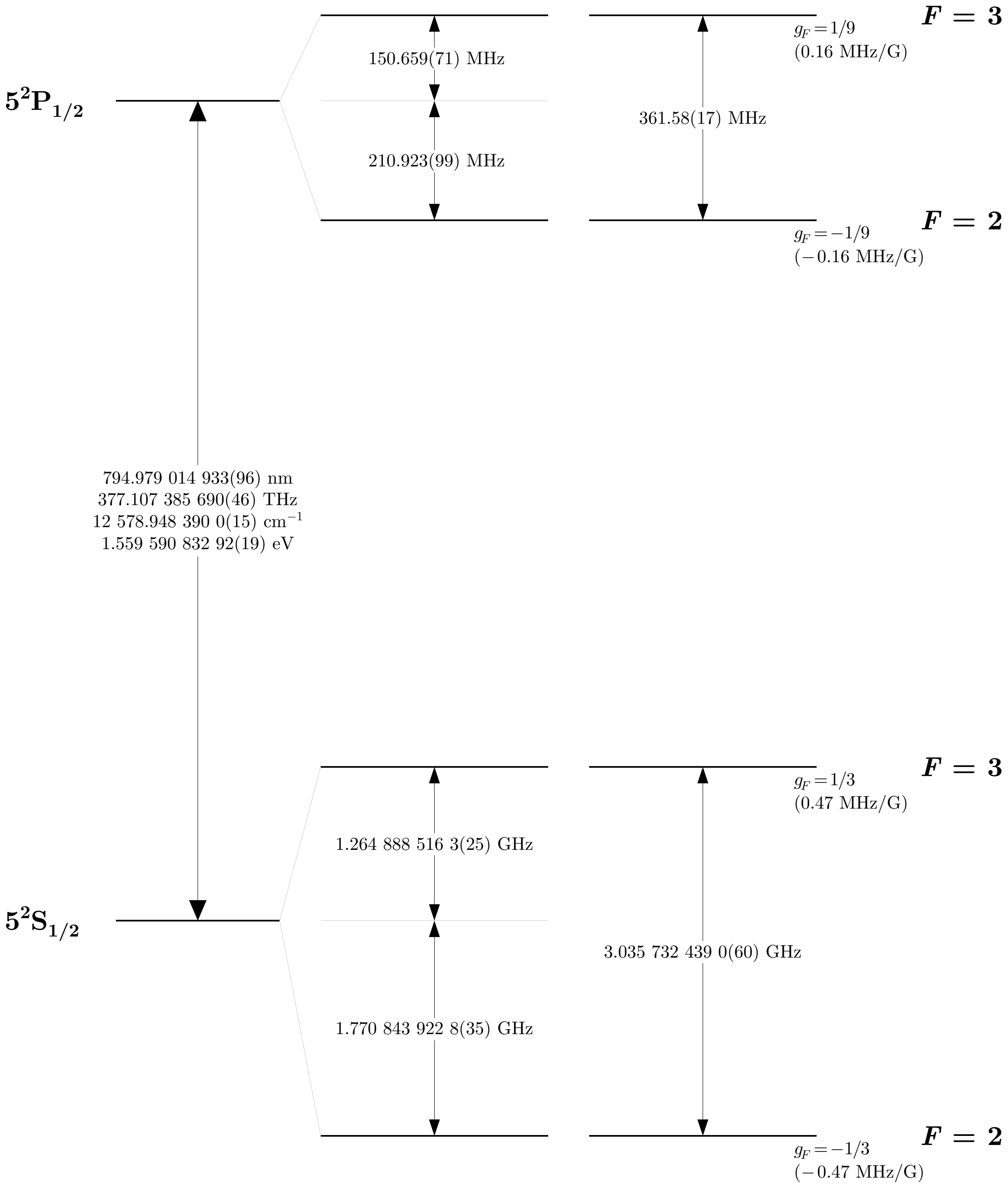

Fig. A.1.2 | ^{85}Rb D_1 transition hyperfine structure, with frequency splittings between the hyperfine energy levels. The approximate Landé g_F-factors for each level are also given, with the corresponding Zeeman splittings between adjacent magnetic sublevels. [2]

A.2 Calculation of Uncertainties Using Gaussian Error Propagation

For uncorrelated variables $x_1, x_2, ..., x_n$ with uncertainties $\sigma_{x_1}, \sigma_{x_2}, ..., \sigma_{x_n}$ and a function $f(x_1, x_2, ..., x_n)$, the uncertainty of f is given by

$$\sigma_f = \sqrt{\sum_{i=1}^{n} \left(\frac{\partial f}{\partial x_i}\right)^2 \sigma_{x_i}^2} \tag{28}$$

A.3 Experimental Setup, Optical Table and Components

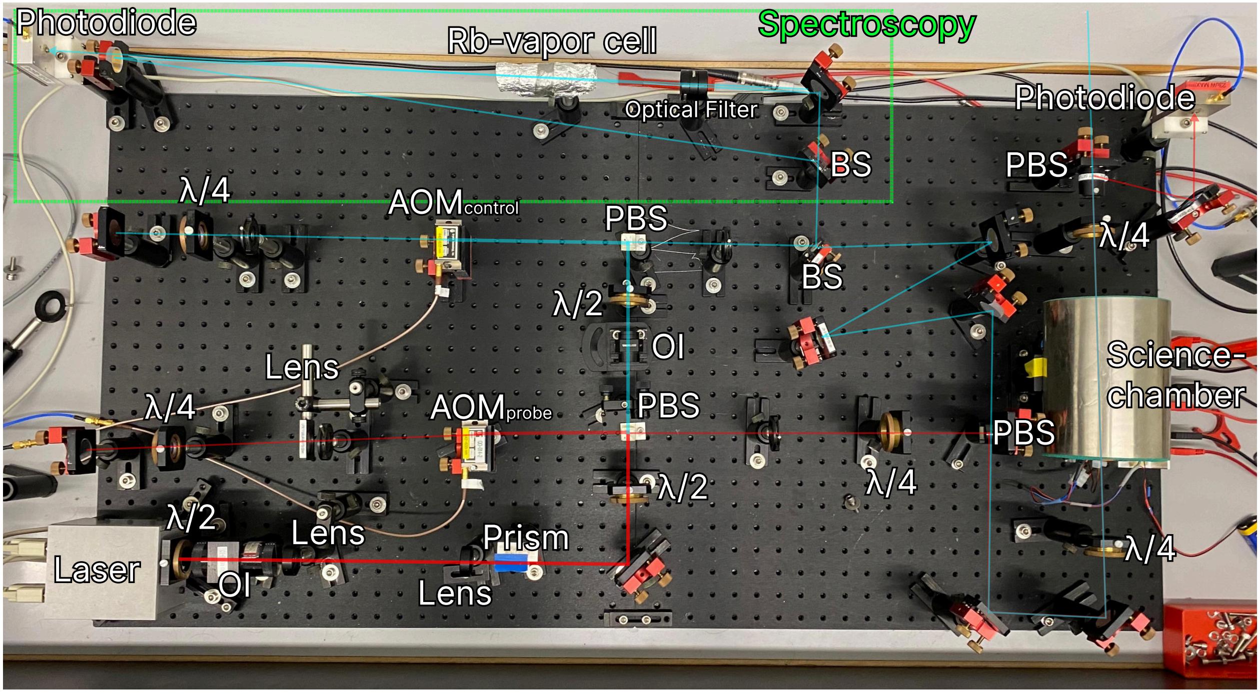

Fig. A.3.1 | Schematic overview of the experimental setup used and explained in the METHODS section. The different beam paths are represented in different colors for visibility and distinguishability. Furthermore all components are labeled with their respective names besides for mirrors and pinholes which are not labeled. Additionally the spectroscopy part is shown in the upper left corner by the dashed box.

A.4 EIT Signal Peak Classification

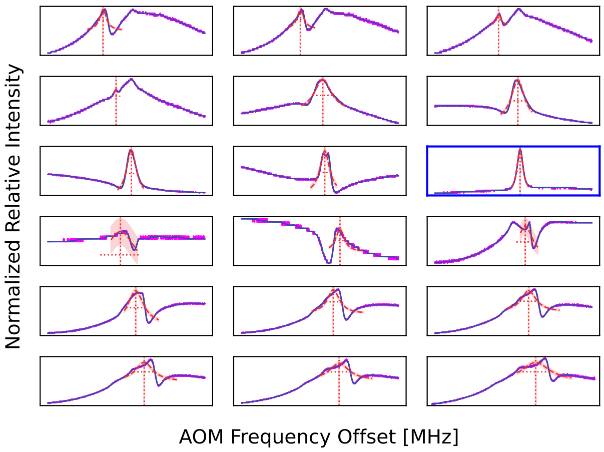

Fig. A.4.1 | EIT signals wit the corresponding peak position and FWHM estimation using Lorentzian fits. The EIT signal is displayed as normalized relative intensity as a function of the AOM frequency offset i.e. detuning of probe and control beams. Furthermore, the plot with the blue border is the one displayed in the RESULTS section above.

A.5 Laser Safety

This experiment involves the use of a diode laser operating at a wavelength of 795nm with a maximum output power of 80mW. The laser falls under class 3B, which poses a significant hazard to the eyes. Since the emitted light lies in the infrared region, it is invisible, increasing the risk of accidental retinal exposure. To ensure safe operation:

- Laser safety goggles appropriate for 795nm must be worn at all times during alignment and operation.
- Beam paths are arranged to be below or above eye level, and care is taken to eliminate reflective surfaces from the setup.
- A laser warning sign is clearly displayed at the laboratory entrance.

By adhering to these safety protocols, the risk of laser-related injury is minimized, and safe experimental conditions are maintained throughout the procedure.

A.6 GW Instek GDS-1022 DSO Data Readout Python Script

```
# Input: Folder structured as follows:
# data/
# |-- measurement1/
# |    |-- ch1 (if acquired)
# |    |-- ch2 (if acquired)
# |    |-- image.bmp
# |    |-- other unnecessary files
# |-- measurement2/
# |-- measurement3/
# ...
#
# Each "measurement" subfolder may contain channels ’ch1’ and/or ’ch2’, a bitmap image, and other files not required for analysis.
#
# Output:
# data[’measurement1’][0] -> ch1 data (if it exists)
# data[’measurement1’][1] -> ch2 data (if it exists)


import numpy as np
import pandas as pd
import os
# import matplotlib.pyplot as plt

# path = input("Please enter the path to the folder: ")

def _is_number(s):
    try:
        float(s)
        return True
    except ValueError:
        return False
    return 0

def csvToArr(file, channel):
    data_ch1 = pd.read_csv(file).to_numpy().transpose()[0, 15:].astype(float)
    labels = pd.read_csv(file).to_numpy().transpose()[0, 0:14].astype(str)
    metadata_ch1 = pd.read_csv(file).to_numpy().transpose()[1, 0:14]
    metadata_dict = {labels[i]: (float(v) if (lambda x: _is_number(x))(v := metadata_ch1[i]) else v) for i in range(len(metadata_ch1))}
    y = (data_ch1 / 25 * metadata_dict[’Vertical␣Scale’]) + metadata_dict[’Vertical␣Position’]
    return y

def read_file(subfolder_path):
    """
        This function reads a csv file and gives back a numpy array.
    """

    # print(subfolder_path)
    os.chdir(subfolder_path)

    files = os.listdir()

    for file in files:
```

```
        if file.endswith(’CH1.CSV’):
            ch1 = csvToArr(file, 1)
            print(ch1)
        elif file.endswith(’CH2.CSV’):
            ch2 = csvToArr(file, 2)
        else:
            print(f"Skipping␣file:␣{file}")

    ch1ch2 = np.array([ch1, ch2])

    return ch1ch2


def read_folder(folder_path):
    folder = os.listdir(folder_path)
    for subfolder in folder:
        # print(os.path.join(folder_path, subfolder))
        # ch1ch2 = read_file(os.path.join(folder_path, subfolder))
        results = {}
        for subfolder in folder:
            ch1ch2 = read_file(os.path.join(folder_path, subfolder))
            results[subfolder] = ch1ch2
        return results

    return 0

path = r"path/to/your/data/folder"  # Replace with your actual path
data = read_folder(path)
```

The script can be found here: `https://n.ethz.ch/~atuzlak/read.py`